OPEN ACCESS

Optimization of Doping Concentration to Obtain High Internal Quantum Efficiency and Wavelength Stability in An InGaN/GaN Blue Light-Emitting Diode

ECS Journal of Solid State Science and Technology, 2023 **12** 076014

Optimization of Doping Concentration to Obtain High Internal Quantum Efficiency and Wavelength Stability in An InGaN/GaN Blue Light-Emitting Diode

Sarai Zarate-Galvez,[1] Abel Garcia-Barrientos,[2,z] Luis Felipe Lastras-Martinez,[1] Marco Cardenas-Juarez,[2] Sharon Macias-Velasquez,[3] Lado Filipovic,[4] and Armando Arce-Casas[5]

[1]*Instituto de Investigación en Comunicación Óptica, Av. Karakorum 1470, 78210, San Luis Potosí, S.L.P., Mexico*
[2]*Faculty of Science, Universidad Autónoma de San Luis Potosí (UASLP), San Luis Potosi 78295, Mexico*
[3]*Faculty of Engineering, Universidad Autónoma de San Luis Potosí (UASLP), San Luis Potosi 78295, Mexico*
[4]*CDL for Multi-Scale Process Modeling of Semiconductor Devices and Sensors, Institute for Microelectronics, TU Wien, Gusshausstrasse 27-29/E360, 1040 Vienna, Austria*
[5]*Cátedras Conahcyt, Universidad Autónoma de San Luis Potosí (UASLP), 78290 San Luis Potosí, Mexico*

We conduct a comprehensive study to investigate the feasibility of achieving high internal quantum efficiency (IQE) and wavelength stability in an InGaN/GaN blue light-emitting diode (LED) through numerical simulations with different doping concentrations. To ensure accurate calculations, we emulated the structure of an LED, fabricated on freestanding GaN with low defect density, abrupt interfaces, and high-performing characteristics, which resemble ideal conditions. Our objective is to determine the optimal doping concentration of the claddings using the Quantum Drift-Diffusion (QDD) model. We tested three concentrations (C_{low}, C_{middle}, C_{high}), and found that C_{middle} produced the highest IQE of 82.5%, the most stable wavelength $\hat{\lambda} = (457.0 \pm 1.2)$ nm in the range of (0.08–63.25) mA, an optical power of $\mathbb{P} = 14.76$ mWs^{-1}, and a forward voltage of $V_{middle} = 3.81$ V at 20 mA. We suggest that using this concentration leads to the parameters closest to those of the reference device.
 [DOI: 10.1149/2162-8777/ace7c4]

Manuscript submitted May 11, 2023; revised manuscript received June 14, 2023. Published July 26, 2023.

Nowadays, many efforts continue to improve the growth and fabrication processes of devices based on group III-nitride semiconductors due to their high impact and potential for the lighting and optoelectronic industry. The widespread technological development is based on the generation of devices using silicon wafers as substrates; therefore, migrating to another material as a structural base is not straightforward. The epitaxial growth of GaN is commonly performed on GaAs, Si, SiC, Al_2O_3, ZnO and other substrates, employing molecular-beam epitaxy (MBE), plasma-assisted MBE (PAMBE), hydride vapor phase epitaxy (HVPE), metal-organic chemical vapor deposition (MOCVD), High Nitrogen Pressure Solution Growth (HNPSG) among other methods.[1–8] Some of the main problems faced by heterostructures with GaN interfaces are crystalline defects and strain, because of the inherent lattice-mismatches. Threading dislocations (TD) are the most detrimental to the device because these passes vertically through the structure, separating material and causing current suppression, carrier leakage and efficiency droop;[3,7,9–11] hence, is desired to obtain GaN with a low defect density. To reduce the dislocation density in the GaN, it is necessary to match the lattice parameters between the GaN film and the substrate, thus many techniques have been developed to address this problem to date, such as the introduction of a buffer layer, epitaxial lateral overgrowth (ELOG) or SiN treatment to make patterned substrate.[3–6,12] Different combinations of structures, materials and techniques are being tested to enhance the light-emitting diode (LED) performance in all colors of the visible spectrum.[13–15] Some researchers have wagered on producing freestanding GaN for the device growth and avoiding, with apparent success, the deterioration of optoelectronic parameters caused by structural defects. For example, Cao et al.[16] studied UV and blue InGaN/GaN LEDs on both sapphire and GaN substrates. Atomic force microscopy (AFM) measurements showed low defects, while the I-V characteristics indicated reduced leakage currents, and internal quantum efficiency reached the highest values for the device manufactured on freestanding GaN. Akita et al.[17] reported higher output power and external quantum efficiency (EQE) for InGaN blue LED structures on GaN than those on sapphire substrates. Moreover, cathodoluminescence (CL) images revealed a threading dislocation density (TDD) which was more than one order of magnitude smaller, when using GaN substrates. Kyle et al.[18] demonstrated that the higher electron mobility in the n-GaN layer on freestanding GaN templates comes from the sample with lower TDD, whereby a improved absorption of donor species was achieved. Defect-free materials such as these, are more easily computer-simulated due to the regular spatial meshing provided and to the fact that they possess near-ideal features; thus, calculating their physical properties can be executed with high accuracy by using computational means prior to cost- and time-intensive manufacture. Lee et al. grew freestanding GaN using HVPE and removing it from Si substrates, resulting in a high-quality material with threading dislocation densities (TDD) in the range of $\sim 1 \times 10^6$ cm^{-2}.[19] Using this freestanding GaN, an InGaN/GaN multiple-quantum-well (MQW) light emitting diode was fabricated. The authors reported a stable and uniform blue wavelength emission ($\lambda = 460$ nm) with red shift about 1 nm in the current range of 0 to 100 mA, an internal quantum efficiency (IQE) of ~80% at room temperature, well-defined transport mechanism and suppression of forward leakage current.[20,21] Since these articles do not indicate the electron and hole concentrations for the n-GaN and p-GaN materials, in this work, three different carrier concentrations (low, middle, and high) are explored to achieve the reported optoelectronic characteristics and establish its viability. Simulations using the Quantum Drift-Diffusion (QDD) model have been performed to compare and verify the parameters of this LED with freestanding GaN by using the Nextnano++ software.[22] The physical outputs which were analyzed include the I-V characteristics, spatial current distribution, recombination processes, current leakage, emission spectrum, peak wavelength stability and internal quantum efficiency.

Methodology

According to Refs. 19–21, the device under study consists of a flat epitaxial structure of InGaN/GaN MQWs fabricated on

[z]E-mail: abel.garcia@uaslp.mx

freestanding GaN by MOCVD. The freestanding GaN was grown on a (111) Si wafer, which produces a wurtzite crystalline structure oriented in the *c*-plane direction.[3,23] The active layer is compounded by four periods of 3 nm thick InGaN QWs and 12 nm thick GaN barrier layers, making the total active layer length 72 nm. At the top and bottom of the active layer, 3.5 μm *n*-GaN and 150 nm *p*-GaN confine the MQWs, respectively. To carry out the simulation, at the edges, 1 nm thick ohmic contacts complete the device as shown in Fig. 1. The InGaN alloy composition is not mentioned in the studies by Lee. However, by extracting data from literature, it is possible to estimate the relative content of GaN and InN to create the InGaN alloy emitting at the given wavelength. For an $In_xGa_{1-x}N$ alloy, the indium relative content reported ranges from $x = (0.13 - 0.21)$ for emissions between $\lambda = (440 - 460)$ nm.[2,11,17,18,24–29] For this work, a low indium content was chosen ($x = 0.15$), resulting in a wavelength about of $\lambda = 456$ nm. The above is because the increase of x implies an increase in indium agglomeration, which produces phase separation in the alloy;[30,31] as well as an increase in the lattice strain, raising the defect density.[1,32] Table I show the electron and hole concentrations for the doped GaN claddings. Here, 100% ionization of acceptors and donors has been assumed and three different concentrations were labeled as "low" (C_{low}), "middle" (C_{middle}) and "high" (C_{high}). Recently, we analyzed the low concentration in another study where other basic material parameters were discussed.[33] The middle concentration was chosen to correspond to the doping in the LED published by Lu et al.[34] to make a comparison with the IQE reported in this paper. The value of C_{high} was chosen by comparing the most common n-GaN devices, consulting several references,[24–26] and approaching the doping values of the study by Zhang et al.[35] Here, $R_{p/n}$ is the ratio between p-GaN and n-GaN concentrations, serving as a proportion indicator between carriers to correlate electrical and optical properties in the device, see Table I. Although a high impurity concentration (Si or Mg) inside any compound semiconductor results in epilayer morphology degradation and surface roughness, the small indium content and low Si impurities used in our study avoids concerns on this issue as discussed by Cavalcoli et al.[36] The high amount of Mg impurities in our case also does not affect the surface morphology due to the small thickness of the n-GaN layer used here. For thicker layers, a proper carrier gas technique during growth can be used to smooth the surface and avoid the Mg diffusion into the active layer.[37,38] In addition, effective techniques to achieve a high Mg concentration such as annealing,[39] cooping,[40] or passivation of the dangling bonds[38,41] have demonstrated to increase the number of Mg ions available for the transport in the device.

To obtain optical and electrical properties from the LED structure in Fig. 1, simulations were done using the Nextnano++ software,[42–45] which employs the local QDD model to calculate charge $[n(\vec{r}, t)]$ and current $[\vec{J}_n(\vec{r}, t)]$ densities[46] as:

$$\begin{cases} \dfrac{\partial}{\partial t} n(\vec{r}, t) - \dfrac{1}{q}\nabla_r \cdot \vec{J}(\vec{r}, t) = 0 \\ \vec{J}_n(\vec{r}, t) = \dfrac{q\tau}{\hat{m}}\left[k_B T_L \nabla_r n - qn\nabla_r V - \dfrac{\hbar^2}{6\hat{m}} n \nabla_r\left(\dfrac{\nabla_r{}^2\sqrt{n}}{\sqrt{n}}\right)\right] \end{cases} \quad [1]$$

In the above equations, q is the electric charge, $\hat{m}$ is the isotropic mass, τ is the scattering average time, T_L is the lattice temperature, V is the electrostatic potential, k_B is the Boltzmann constant, and $(\nabla_r^2\sqrt{n}/\sqrt{n})$ is interpreted as a quantum potential (Bohm potential). Note that if $\hbar^2 \to 0$ the equations are reduced to the classical drift diffusion (CDD) model, therefore equations in (1) are satisfied in all the semiconductor domains. This means, the CDD may be employed in the device regions where the semi-classical model (with $\hbar^2 \to 0$) dominates, this is, outside the active layer of the device. The QDD model is taken in domains where quantum mechanical effects are relevant (taken $\hbar^2 \neq 0$), i.e., in the MQWs. The generation-recombination processes $[G(\vec{r})/R(\vec{r})]$ considered within the entire LED were: 1) Schockley-Read-Hall (SRH), 2) Auger and 3) radiative. Since there is no additional external excitation, $G(\vec{r})$ will be zero. Additionally, if stationary solutions are assumed $[\dot{n}(\vec{r}) = \dot{p}(\vec{r}) = 0]$, the continuity equations for electrons (n) and holes (p) are:

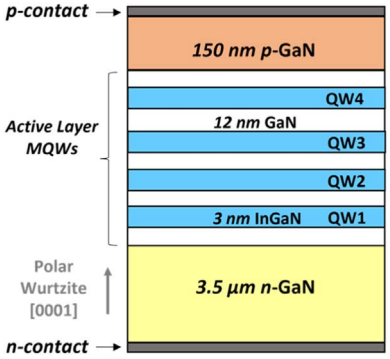

Figure 1. Schematic structure for simulations of InGaN/GaN blue LED based in Lee's device.[20]

$$\begin{cases} \dfrac{\partial}{\partial t} n(\vec{r}) - \dfrac{1}{q}\nabla_r \cdot \vec{J}_n(\vec{r}) = -R(\vec{r}) \to \dfrac{1}{q}\nabla_r \cdot \vec{J}_n(\vec{r}) = R(\vec{r}) \\ \dfrac{\partial}{\partial t} p(\vec{r}) + \dfrac{1}{q}\nabla_r \cdot \vec{J}_p(\vec{r}) = -R(\vec{r}) \to \dfrac{1}{q}\nabla_r \cdot \vec{J}_n(\vec{r}) = -R(\vec{r}) \end{cases} \quad [2]$$

For the classical case and using the mobility expression $\mu_{n,p} = (q\tau/\hat{m}_{n,p})$, the current equations may be written in terms of the gradient of quasi-Fermi levels $E_{F,n/p}(\vec{r})$ instead of the electrostatic potential as:

$$\begin{cases} \vec{J}_n(\vec{r}) = \mu_n[qn\nabla_r E_{F,n} + k_B T_L \nabla_r n] \\ \vec{J}_p(\vec{r}) = \mu_p[qp\nabla_r E_{F,p} - k_B T_L \nabla_r p] \end{cases} \quad [3]$$

Therefore, the governing dynamic equations in combination with the Poisson equation are:

$$\begin{cases} \nabla_r \cdot \vec{J}_n(\vec{r}) = \nabla_r \cdot [q\mu_n n\nabla_r E_{F,n} + \mu_n k_B T_L \nabla_r n] = qR(\vec{r}) \\ \nabla_r \cdot \vec{J}_p(\vec{r}) = \nabla_r \cdot [q\mu_p p\nabla_r E_{F,p} - \mu_p k_B T_L \nabla_r n] = -qR(\vec{r}) \end{cases} \quad [4]$$

These are solved self-consistently with proper boundary conditions. The constant mobility model[47–50] for electron and hole mobilities (μ_n, μ_p) is used in calculations by the equation:

$$\mu_{n,p}(T) = \mu_{\max}^{n,p}(T_0)\left[\frac{T}{T_0}\right]^{\alpha_{n,p}} \quad [5]$$

In (5), $\mu_{\max}^{n,p}$ is the maximum mobility due to bulk phonon scattering for electrons or holes, T is the lattice temperature, $T_0 = 300$ K, and $\alpha_{n,p}$ is the power value corresponding to the best approximation to the experimental data for the semiconductor. In the constant mobility regime, the saturation velocity for the material is used. In this way, Eq. 3 from R. Quay[48] for the saturation velocity can be adapted to the alloy mobility as:

$$\mu_{AB} = x \cdot \mu_A + (1 - x) \cdot \mu_B \quad [6]$$

The relative contents are $x = 0.15$ and $(1 - x) = 0.85$; μ_{AB}, μ_A, and μ_B correspond to the alloy and precursors mobilities, respectively. Since the $In_xGa_{1-x}N$ alloy is created through the precursor nitrides: GaN and InN, μ_{InN} and μ_{GaN} are used to calculate μ_{InGaN} via Eq. 6 for both holes and electrons; thus, the $In_{0.15}Ga_{0.85}N$ mobility is also

Table I. Doping concentrations from n/p type GaN claddings for the blue LED simulations.

Concentration	C_{low}	C_{middle}	C_{high}
n-GaN [cm^{-3}]	1×10^{17}	2×10^{18}	5×10^{18}
p-GaN [cm^{-3}]	1×10^{19}	1×10^{19}	2×10^{19}
$R_{p/n}$	100	5	4

constant for each simulation. To strengthen the mobility model, μ_n / μ_p values were taken from literature, including the doping concentration dependence on the three GaN concentrations proposed in Table I, this data is shown in Table II. Because only electron and hole concentrations change for the GaN claddings, electron and hole mobilities will be the same for InN in all three simulations: $\mu^n_{InN} = 3200\ cm^2\,V{\cdot}s^{-1}$ [51–53] and $\mu^p_{InN} = 220\ cm^2\,V{\cdot}s^{-1}$,[54] which corresponds to intrinsic InN.

Moreover, spontaneous (SP) and piezoelectric polarization (PZ) will contribute to displace the band structure in the device, which may be included in the equations as deformation potentials during the simulation in order to include its effects. Since GaN has a wide bandgap, the conduction and valence bands are treated separately, thus the single-band effective mass approximation is used for the Gamma conduction band and for the heavy-hole (hh), light-hole (lh), and spin–orbit (so) valence bands.

The radiative recombination will describe the spontaneous photon emission,[2,24] which is governed by Fermi's golden rule as:

$$R^{spon}_{rad}(x, E) = B(x) \int dE_V \int dE_C n(x, E_C) p \times (x, E_V)\delta(E_C - E_V - E) \quad [7]$$

$B(x)$ is the radiative recombination parameter, specific to the material, while $n(x, E_C)$ and $p(x, E_V)$ are the charge densities. Equation 7 represents the energetic transitions between electron and hole states. Therefore, the sum of the most probable and fastest transitions will form the total spectrum at different potential values. The broadening induced by intraband transitions in the emitted spectrum will be represented with a Lorentzian function. The total radiative recombination of charge on the active layer volume may be associated with a current called photocurrent, which is defined as:

$$J_{photo} = q \int R^{spon}_{rad}(\vec{x}) dV \quad [8]$$

In concordance to the ABC model,[59] the total current may be expressed as the superposition of current densities associated to radiative and non-radiative processes ($J_{tot} = J_{rad} + J_{non-rad} = J_{photo} + J_{SRH} + J_{Aug}$), where each partial current will satisfy the functional form of Eq. 8 but with their respective recombination ratios. To consider leakage currents and the percentage between radiative and non-radiative processes in the active layer of the device, the internal quantum efficiency (IQE, η_{IQE}) can be expressed via the total current and photocurrent as:

Table II. Mobility values corresponding to n/p doping concentration in GaN claddings.

Binary compound	Mobility [cm^2/V·s]		
	C_{low}	C_{middle}	C_{high}
GaN	$\mu_n = 1035$[55,56] $\mu_p = 30$[57,58]	$\mu_n = 300$[55] $\mu_p = 30$[57,58]	$\mu_n = 200$[55] $\mu_p = 25$[57,58]

$$\eta_{IQE}[\%] = \frac{J_{photo}}{J_{Tot}} \times 100 \quad [9]$$

The discontinuity between interfaces in the discretized equations is represented by a box integration finite difference approach during the simulation. A variable spatial grid in one dimension was employed. For the first 3500 nm n-GaN and the last 150 nm p-GaN the spatial resolution was $\Delta x = 10$ nm, for the active layer $\Delta x = 0.1$ nm. A voltage sweep was applied with step sizes of $\Delta V = 0.05$ V until the point where the simulation convergence fails, which corresponds to the cut-in voltage point. Values for the recombination coefficients and others simulation parameters may be consulted in Refs. 33–60. All calculations were performed at 300 K.

Results and Discussion

Figure 2 shows the forward I-V characteristics for the three doping concentrations. A transversal area of 350 μm × 350 μm on the LED was assumed for calculations as a Ref. 21. In Figs. 2a and 2b, the total current and photocurrent are plotted on a logarithmic scale to clearly observe the changes in transport mechanisms and the activation of radiative recombination processes. These changes are evaluated by comparing the ideality factor value (n) in each voltage region to which the LED is subjected.[3] The ideality factor (n) incorporates all the unknown effects which make the device non ideal, and its value indicates which transport mechanisms are active in the diode. If (n) is between 1 and 2, the current is mainly dominated by diffusion and recombination process, while if (n) is much larger than 2, the carriers are governed by tunnelling mechanisms.[21,61,62] Using the Schockley equation[61,62] three distinct regions on the graph can be observed, labeled (I, II, III). Region I, below 2.50 V is governed by tunneling processes, with the ideality factor (n) > 50. In region II with bias between (2.50−3.50) V, radiative recombination processes are turned on and (n) decreases significantly. Region III is representative of a bias above 3.50 V, where the processes of recombination and diffusion coexist, increasing the current; here the ideality factor ranges between (5.0 −4.3). Comparing (n) for the different doping concentrations, C_{middle} curve has the largest value ($n^{I}_{C_{middle}} \approx 57.4$) in the first region. This means that C_{middle} reveals the smallest slope, which can be attributed to less tunneling due to an appropriate combination of doping ($R_{p/n} = 5$) which maintains a similar size between electron and hole depletion region widths generating more balanced charge densities within the active layer. In the central region, C_{high} reaches the steepest slope with $n^{II}_{C_{high}} \approx 10.0$, indicating that many electron and hole pairs are being recombined. For region III, C_{middle} outperforms the others curves with $n^{III}_{C_{middle}} \approx 4.3$ and, being the ideality factor $n_{Ref} \approx 4.5$ of the reference device[21] in region III, the middle concentration is the closest to this value. Other similar devices fabricated on sapphire substrates have factors of $n_{saph} \approx (6.2 - 1.9)$;[21,62] therefore, the three concentrations studied fall within this range. We should also make it clear that, in the experiments, a low (n) is associated with low defect densities. For simulations such as this work, where the mesh is uniformly distributed, low ideality factors in this voltage zone should be expected. On the other hand, Fig. 2a indicates the total current is highest for C_{low} in region I. This is because the recombination processes are the lowest at this concentration (see Fig. 2b). This concentration also has high hole availability, tunneling through the active layer up to QW1, thereby avoiding recombination within other wells (Fig. 5b and 9 in Ref. 33), thus many carriers leak out. For this reason, a non-linear behavior is observed below 2.50 V in Fig. 2b. This behavior extends to half of region II and remains below the other two currents until the region III. On the contrary, the current magnitude increases for C_{high} and C_{middle} in region II due to the increment in the radiative processes, as

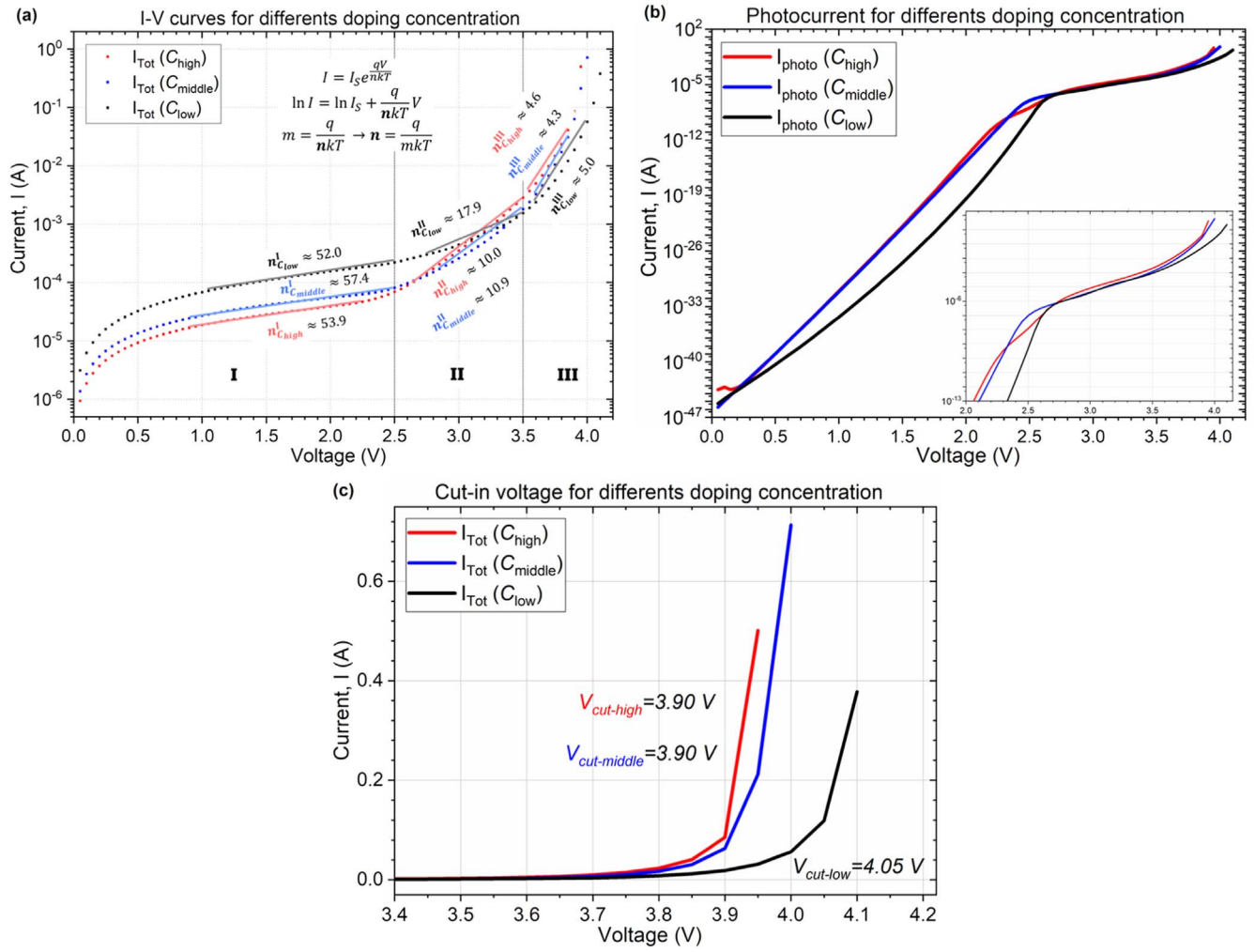

Figure 2. (a) Total current, (b) photocurrent, and (c) cut-in voltage for the three simulated doping concentrations in forward bias for the $In_{0.15}Ga_{0.85}N$/GaN LED.

shown in photocurrent graph. Figure 2b shows the generation of photons activating from the first voltage points, but with very low values. A slope change occurs above 2.50 V, indicating the radiative recombination has acquired enough carriers to increase the number of photons to be physically measurable. The zoom of the photocurrent plot shows C_{low} and C_{middle} having the same values from 2.70 V to 3.50 V, but C_{high} reaches slightly larger values because it has large hole number (p-GaN $= 2 \times 10^{19}$ cm^{-3}), which dominates the transport in this range.[61] However, after 3.50 V, the photocurrent of C_{middle} approaches C_{high} up to the cut-in-voltage point. Figure 2c shows the cut-in voltage for the three concentrations precisely, according to the linear fits made in region III of Fig. 2a. The next upper point to the voltage end point contributing to the straight line, will be the critical or "knee" point of the device. This point separates the curve of small and large current variations as shown in such a graph, resulting in $V_{cut-low} = 4.05$ V, $V_{cut-middle} = V_{cut-high} = 3.90$ V.

Figures 3–5 depict the spatial distribution of the current and recombination within the active layer of the LED in the final points of each region described above. Figure 3 corresponds to 2.50 V in region I for the three concentrations. For C_{low} the hole and electron currents remain constant, i.e., the total current of the device is not reduced when crossing the QWs. This means the three recombination processes are very low at this point as illustrated in Fig. 3b. There, only the first well exhibits significant recombination mechanisms, being the SRH recombination ratio (R_{SRH}) one order of magnitude greater than radiative recombination (R_{rad}). For C_{middle} the current distribution is no longer constant. Figure 3c displays the first two wells participating in current consumption; Fig. 3d shows R_{SRH} in the first three wells, and R_{rad} only in the first two. Moreover, the magnitude of both total recombination values (R_{rad}^{tot} and R_{SRH}^{tot}) increases by two orders of magnitude with respect to the previous concentration. For C_{high} the current consumption is present in the first three wells (see Fig. 3e). The plot in Fig. 3f shows both recombination mechanism reaching QW4 but in a smaller proportion, R_{SRH} decreases and R_{rad} increases as the electron transport migrates to p-GaN. There, R_{rad}^{tot} is lower than the one recorded for the middle concentration, indicating that the higher photon efficiency at this voltage point, is achieved by C_{middle}.

The point at 3.50 V is extracted to show the final stage of the recombination and current consumption inside the wells in region II. The three simulated concentrations are presented in Fig. 4, one of the main differences seen in graphs (a), (c), and (e) is in the current magnitudes entering and leaving the active layer, electron current is higher at the beginning and lower at the end as the doping concentration increases. This implies a decrease in carrier leakage and a rise in total recombination. The recombination plots reveal the highest R_{SRH} and R_{rad} rates for C_{low} and C_{high} are emerging in QW4, and for C_{middle} in QW1 and QW4. Auger recombination (R_{Aug}) is very low in this voltage range, therefore it is not shown. Plots (b), (d) and (f) of Fig. 4 indicate the R_{SRH} predominates by an order of magnitude over R_{rad} during the interaction processes. Although R_{rad}^{tot} is higher for C_{high} in Fig. 4f, C_{middle} is the one achieving a more balanced distribution of the dispersive processes in the four wells (Fig. 4d).

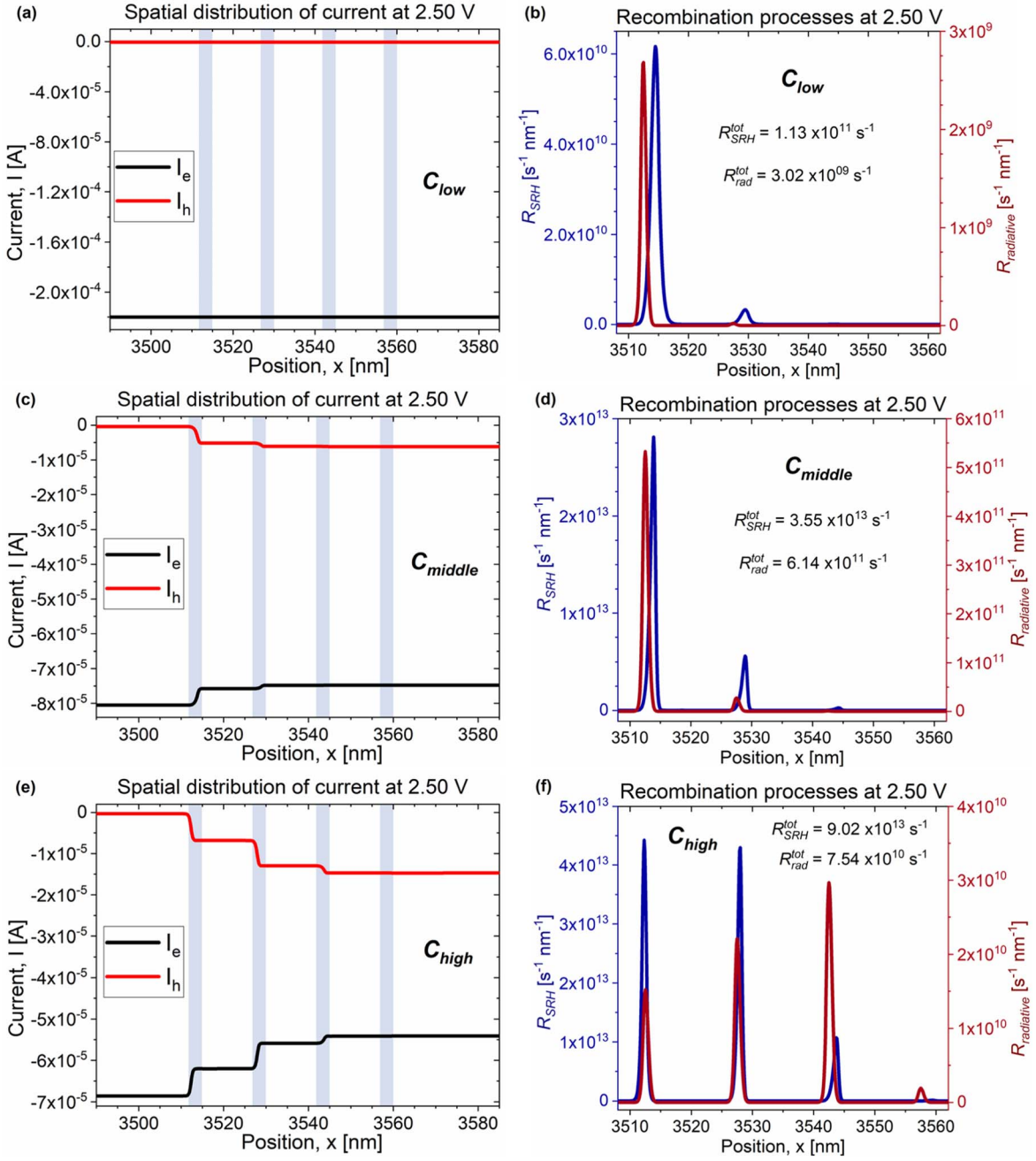

Figure 3. Spatial distribution current and recombination processes in QWs for C_{low} (a), (b), C_{middle} (c), (d), and C_{high} (e), (f) at 2.50 V on the $In_{0.15}Ga_{0.85}N$/GaN LED, respectively.

To describe the carrier behavior prior to LED breakup in region III, the point at 3.90 V is displayed in Fig. 5. For C_{low} and C_{middle} the highest charge recombination occurs in the same wells as in the previous voltage point and, for C_{high} the QW1 is included, making it very similar to C_{middle}. In addition, Auger recombination is included here, since its own nature indicates that increasing the carrier speed will increase the collision probability and energy loss with another nearby particle. Since R_{Aug} is proportional to the charge density to the third order (n^3), it is relevant at high currents. To achieve optimal photon emission values, R_{Aug} should be kept at low levels or close to R_{SRH} according to the ABC model, as other authors have previously mentioned.[2,59,63] Moreover, the rise of R_{Aug} causes "the droop efficiency" in LEDs;[24,59,63–66] therefore, finding the appropriate $R_{p/n}$ combination with lower Auger recombination is desired for our study. In this way, the lower R_{SRH}/R_{Aug} ratio will produce a higher R_{rad} C_{high}, whose ratio is given by $R_{SRH}/R_{Aug} = 31$ which is calculated by comparing the total recombination rates in plots at 3.90 V. However, it is important to note that this voltage point is the penultimate for this concentration (see Fig. 2c), since later, the solution of coupled equations diverge. Thus, it is most appropriate to compare the maximum radiative recombination value reached by each concentration, which contrasts the maximum IQE values, reached just before the simulation fails.

By studying the I-V curves, three voltage points (2.70, 3.15 and 3.40) are found in region II, where currents coincide in magnitude for two different concentrations; hence, a comparison of the electron and hole leakage currents between them can be made. In 2.70 V, C_{high} and C_{middle} have similar total current magnitudes

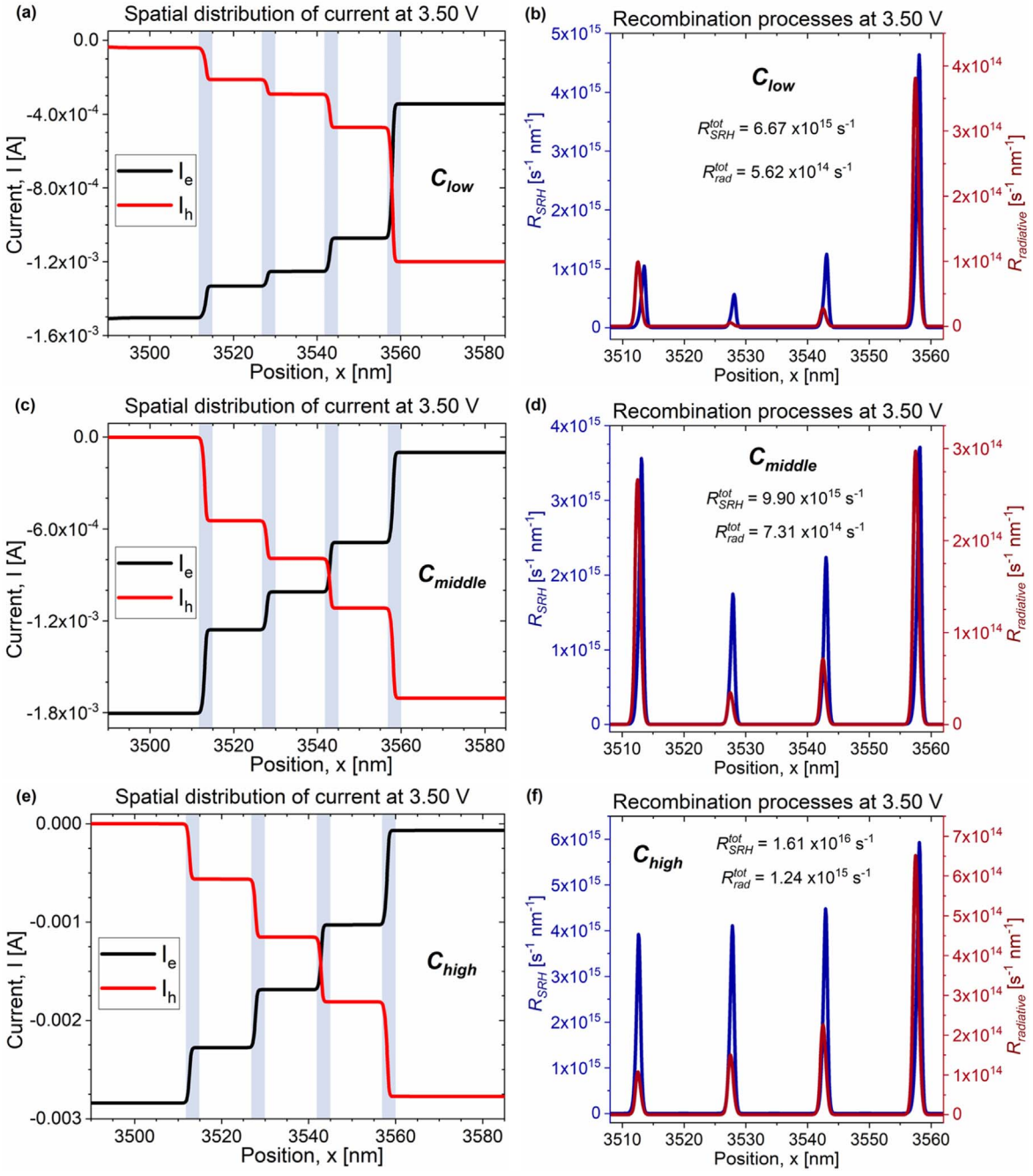

Figure 4. Spatial distribution current and recombination processes in QWs for C_{low} (a) (b), C_{middle} (c), (d), and C_{high} (e), (f) at 3.50 V on the $In_{0.15}Ga_{0.85}N$/GaN LED, respectively.

($I_{high} = 1.21 \times 10^{-4}A$, $I_{middle} = 1.19 \times 10^{-4}A$). Figure 6a shows how the electron current for both concentrations enter the first well; nevertheless, the current consumption for C_{middle} focuses on the first three wells, whereas in C_{high}, the current consumption increases as it approaches the "p-GaN" layer. The greatest amount of recombination occurs in the well where the current step is highest, which occurs in QW1 for C_{middle} and in QW3 for C_{high}. The electron and hole current leakage for these concentrations are shown in Fig. 6a, where C_{high} presents a higher carrier hoarding in the active layer. However, the above does not mean that it is better than middle concentration since, the maximum R_{rad} achieved is by C_{middle} in QW1 according to Fig. 6b. There, the total recombination is higher for C_{middle}, implying carrier loss in C_{high} by non-radiative recombination (SRH in QW3). This can be explained by recalling the probability of recombination processes taking place and being maximized depends on the carrier concentration moving through the active layer as stated in Eq. 7. Since the increase in charge density generates Coulomb repulsion between particles within the flow, producing an additional perturbative potential dampens or screens the total electrostatic potential.[67] Thus, the non-radiative dispersion ratio will increase, prevailing over the R_{rad} of the electron-hole pair. The photocurrent reaches a higher value at this voltage point for C_{middle} ($I^{middle}_{photo} = 6.20 \times 10^{-7}A$), confirming its superiority over C_{high} ($I^{high}_{photo} = 5.15 \times 10^{-7}A$) as illustrated in Fig. 2b. For 3.15 V the total current values in C_{high} and C_{low} are equivalent ($I_{high} = I_{low} = 6.19 \times 10^{-4}A$). Figure 6c displays leakage currents, where about 99% of the carriers are recombining in the

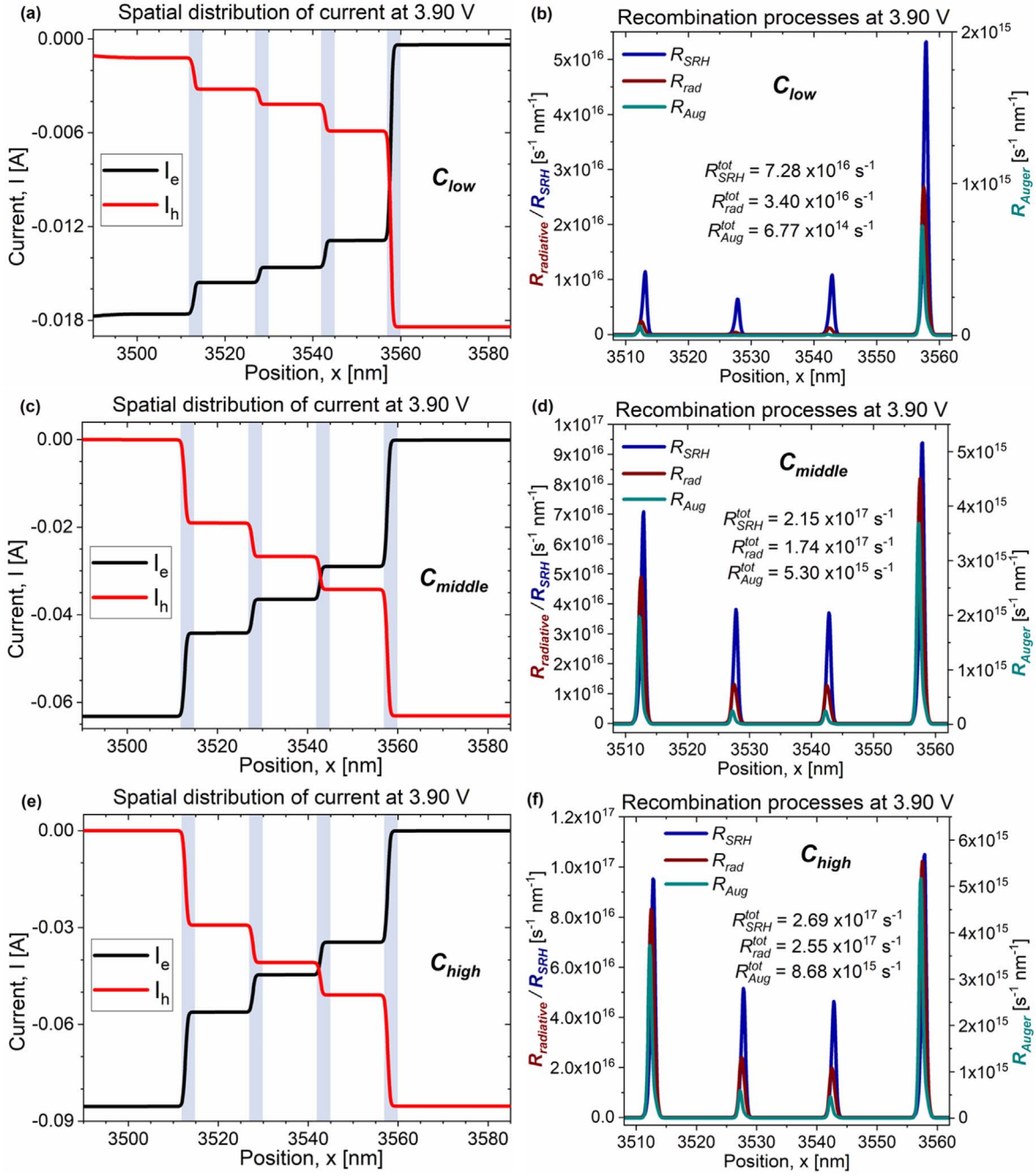

Figure 5. Spatial distribution current and recombination processes in QWs for C_{low} (a) (b), C_{middle} (c, d), and C_{high} (e, f) at 3.90 V on the $In_{0.15}Ga_{0.85}N$/GaN LED, respectively.

active layer for C_{high}. In this concentration, although the highest current step is generated at QW3 and currents cross, does not have the maximum peak of R_{rad} (Fig. 6d), meaning the SRH recombination is consuming the largest number of carriers there. Photocurrent data supports the claim that the radiative recombination is higher for C_{high} ($I^{high}_{photo} = 2.01 \times 10^{-5}A$) than for C_{low} ($I^{low}_{photo} = 1.21 \times 10^{-5}A$), which is also reflected in the R^{tot}_{rad} shown in Fig. 6d. For 3.40 V, the low and middle concentrations are those reaching equivalent current values ($I_{middle} = 1.09 \times 10^{-3}A$, $I_{low} = 1.10 \times 10^{-3}A$). In Fig. 6e, C_{low} presents a large current step in QW4 and such recombination produces the maximum photon peak (see Fig. 6f); despite this, its R^{tot}_{rad} is less than C_{middle} as is confirmed by photocurrent data: $I^{low}_{photo} = 4.66 \times 10^{-5}A$ and $I^{middle}_{photo} = 5.33 \times 10^{-5}A$. The lowest electron and hole leakage currents are registered by C_{middle}, having two pronounced current steps in QW1 and QW4, which produce high radiative recombination, meaning a more equilibrated and stable R_{rad} distribution there.

The simulations were aimed to achieve the highest internal quantum efficiencies by using Eq. 9, to report the viability of reaching the 80% of IQE mentioned by authors Lee et al. in Ref. 20. Thus, all three simulations were ramped up to a critical voltage point where the QDD diverge; such points correspond to (3.95, 4.00 and 4.10) V for high, middle, and low concentrations, respectively. Maximum efficiencies achieved resulted in: $\eta^{high}_{IQE} = 82.0\%$, $\eta^{middle}_{IQE} = 82.5\%$ and $\eta^{low}_{IQE} = 60.4\%$; consequently C_{middle} and C_{high} achieve the desired IQE. Comparing the efficiency of the middle concentration with a similar structure reported by Lu et al.,[34] where

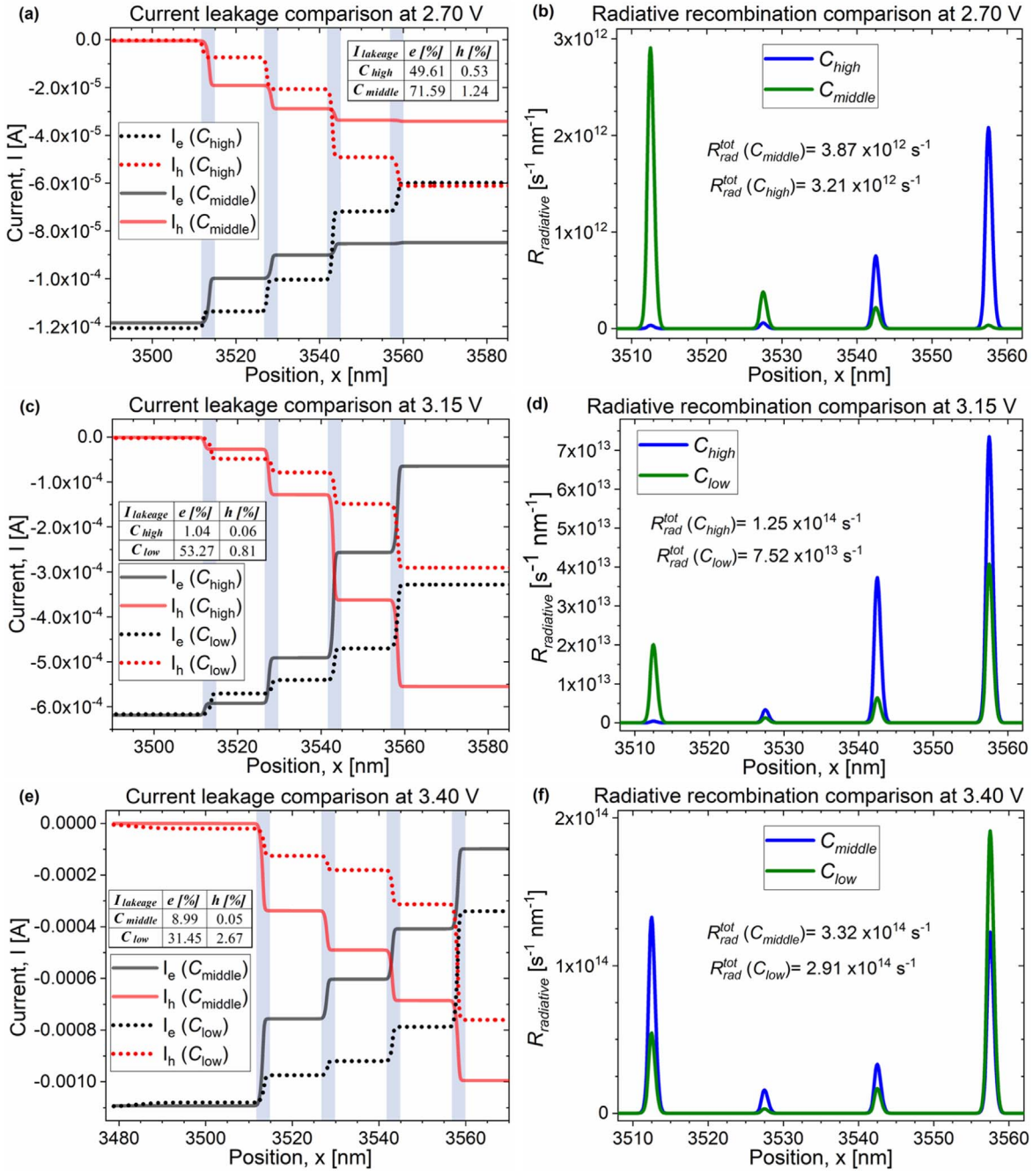

Figure 6. Current leakage and radiative recombination at 2.70 V (a) (b), 3.15 V (c), (d), and 3.40 V (e), (f) on the $In_{0.15}Ga_{0.85}N$/GaN LED, respectively.

the number of QWs was varied for the indicated 3- and 5-MQWs structures, the maximum IQE were found to be 69% and 62%, respectively. The efficiency achieved by our 4-MQWs device is approximately 17% higher than those. Based on these results, spontaneous emission spectra for each simulation were analyzed and compared, first for the three previously analyzed voltage points (2.50 V, 3.50 V, and 3.90 V) and subsequently for the spectrum evolution of each concentration.

Figure 7 show the average wavelength of the maximum peak ($\hat{\lambda}_{max}$), the full width at half maximum (FWHM), photon number emitted (γ) and the optical power for each concentration. The spectra are not presented to scale in order to better observe their differences with respect to the above parameters. As additional comparison data, the current reached at each concentration is displayed. At 2.50 V (Fig. 7a) a violet shift of $\hat{\lambda}_{max}$ is observed as the doping concentration increases in the claddings, which is due to the increase in filling of the energy states by electrons in the quantum wells, since more carriers are available. Thus, the electron-hole pair recombination occurs from a larger energy difference, generating photons with shorter wavelength. The widest FWHM is obtained by C_{low}, which can be attributed to the highest $R_{p/n} = 100$ ratio at this concentration, since having many holes and few electrons available, makes recombination slow and from lower energy levels, explaining the low number of emitted photons. C_{middle} reaches the highest number of photons and a narrow FWHM, possessing the most efficient recombination ratio, as previously noted in Fig. 3d. In terms of optical output power, this was adjusted according to the full LED area $(350\ \mu m)^2$, thus, the maximum power reached was for C_{middle} with $\mathbb{P} = 0.27\ \mu W/s$. At 3.50 V (Fig. 7b) the spectra of C_{middle} and

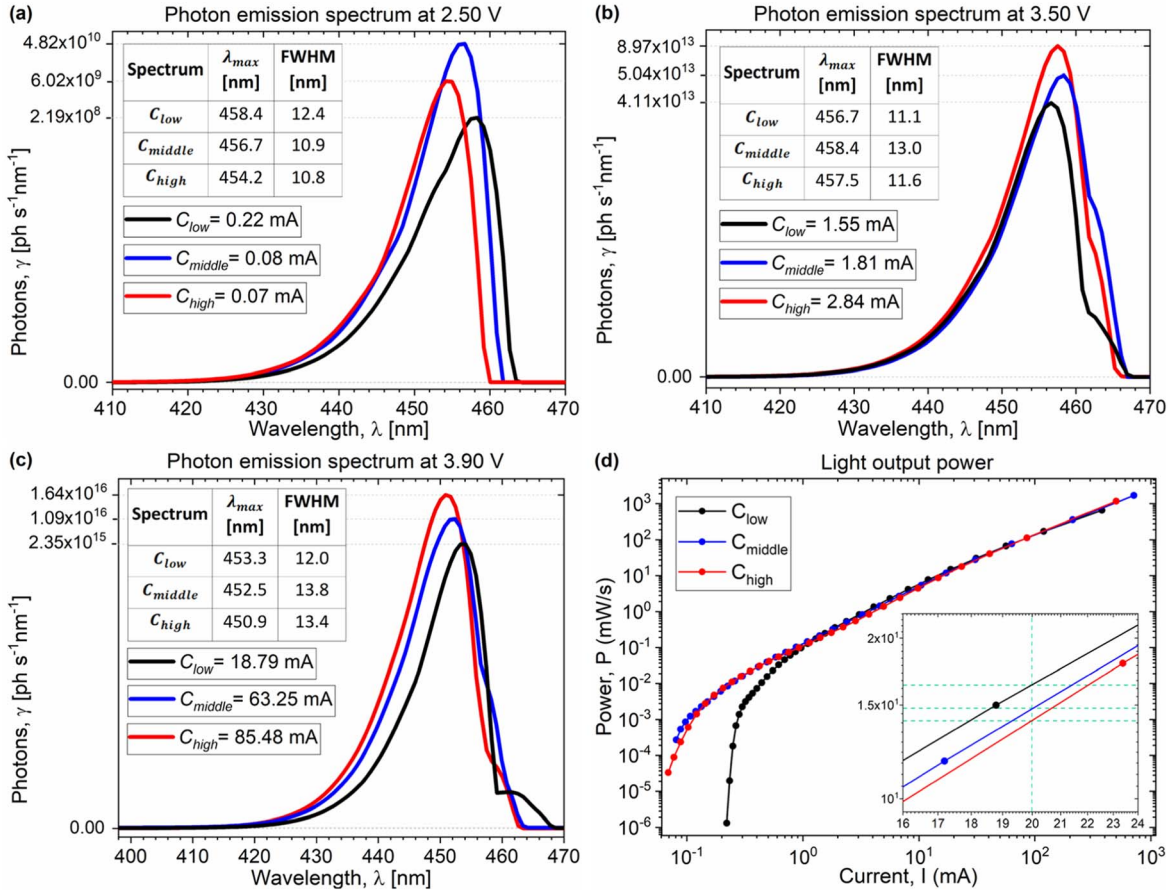

Figure 7. Photon emission spectrum comparing maximum peak of wavelength, FWHM and photon number for each concentration at (a) 2.50 V, (b) 3.50 V, and (c) 3.90 V. (d) Light output power from 2.5 V to the last convergent voltage point for the three concentrations in the $In_{0.15}Ga_{0.85}N/GaN$ LED.

C_{high} have a wider FWHM; this broadening is due to the presence of several Lorentzian peaks forming the spectrum. For the three curves, the existence of a blue peak (between $\lambda = [460–466]$ nm) at the right extreme of the graph is notable, corresponding to the lowest energy transitions in the wells. Such a peak is higher for C_{middle} than for C_{low} and C_{high}; therefore, it will be more evident in the spectrum deconvolution (Fig. 9). Additionally, here the wavelengths are similar to each other, indicating a higher LED emission stability. The number of photons increases for more than three orders of magnitude with respect to the previously analyzed voltage and the maximum power of $\mathbb{P} = 0.54$ mW/s is achieved by C_{high}. In Fig. 7c a widening of the FWHM, a violet shift, and an increase in the number of photons by three orders of magnitude in the spectrum is again observed. The highest optical power is preserved by C_{high} with $\mathbb{P} = 0.11$ W/s. Finally, Fig. 7d shows the light output power vs current at the functional current of 20 mA. Powers of $\mathbb{P}_{low} = 16.37$ mW/s, $\mathbb{P}_{middle} = 14.76$ mW/s, and $\mathbb{P}_{high} = 14.04$ mW s^{-1}, as well as the forward voltages of $V_{low} = 3.91$ V, $V_{middle} = 3.81$ V, and $V_{high} = 3.78$ V are reached for C_{low}, C_{middle} and C_{high}, respectively. The highest power is recorded for C_{low} because the voltage at this current point is larger and the wavelength shorter than the other two concentrations. The forward voltage and optical power recorded by Lee et al. at 20 mA are 3.65 V and 14.9 mW for a wavelength of 460 nm, respectively.[20] Therefore, the optical power characteristics of C_{middle} best match with the reference publication, although our voltage exceeds it by 0.16 V.

The spectrum evolution and the maximum peak wavelength with respect to voltage changes are presented in Fig. 8. In Fig. 8a the C_{low} spectrum is displayed, showing one spectrum for each change of $\hat{\lambda}_{\max}$ recorded. This first concentration has eleven wavelength variations, starts with $\lambda = 458.4$ nm at 2.50 V and the spectrum shifts to the violet wavelengths continuously as the voltage in the simulation increases up to $\lambda = 435.8$ nm at its critical point of 4.10 V. Between (3.40−3.80) V the spectrum is well defined and stable, at 3.40 V the spectrum shows the blue peak separation discussed above, which remains in the subsequent spectra. In Fig. 8b the spectrum evolution for C_{middle} shows nine wavelength changes beginning with $\lambda = 456.7$ nm at 2.50 V and ending with $\lambda = 435.0$ nm at 4.00 V. At this concentration, greater spectrum stability is observed, because $\hat{\lambda}_{\max}$ does not change from (2.50–3.25) V. The constant emission width region is between (3.25–3.75) V. During this voltage period, the discussed blue peak rises as a hump in the spectrum remaining throughout the simulation. In general, the spectrum shows a slight red shift and results in shifting towards violet, whose shift is more pronounced than for the previous concentration. In Fig. 8c the spectrum evolution for C_{high} is presented, where the wavelength varies by ten times and the blue peak bulge is noticeable at 3.15 V. There, emission starts with $\lambda = 454.2$ nm at 2.50 V and concludes with $\lambda = 437.3$ nm at 3.95 V. From (3.15−3.70) V the spectrum maintains its shape and it is stable. The redshift is also observed before the direction change towards violet, whose last jump in the spectrum is very pronounced. Figure 8d displays all $\hat{\lambda}_{\max}$ for each voltage step in the simulation; here the zigzagging of the emissions and their deviation at the last voltage points is notable. The red shift is typical of the Quantum-Confined Stark Effect (QCSE), which bends the semiconductor valence and conduction bands, leading to a physical separation of the electron and hole wavefunction. This reduces the recombination probability in the QWs, which in turn, leads to reduced emission efficiencies.[68,69] In this plot, the skewing and broadening of the spectrum at all three concentrations is more remarkable. Nevertheless, this effect is more pronounced in C_{high}

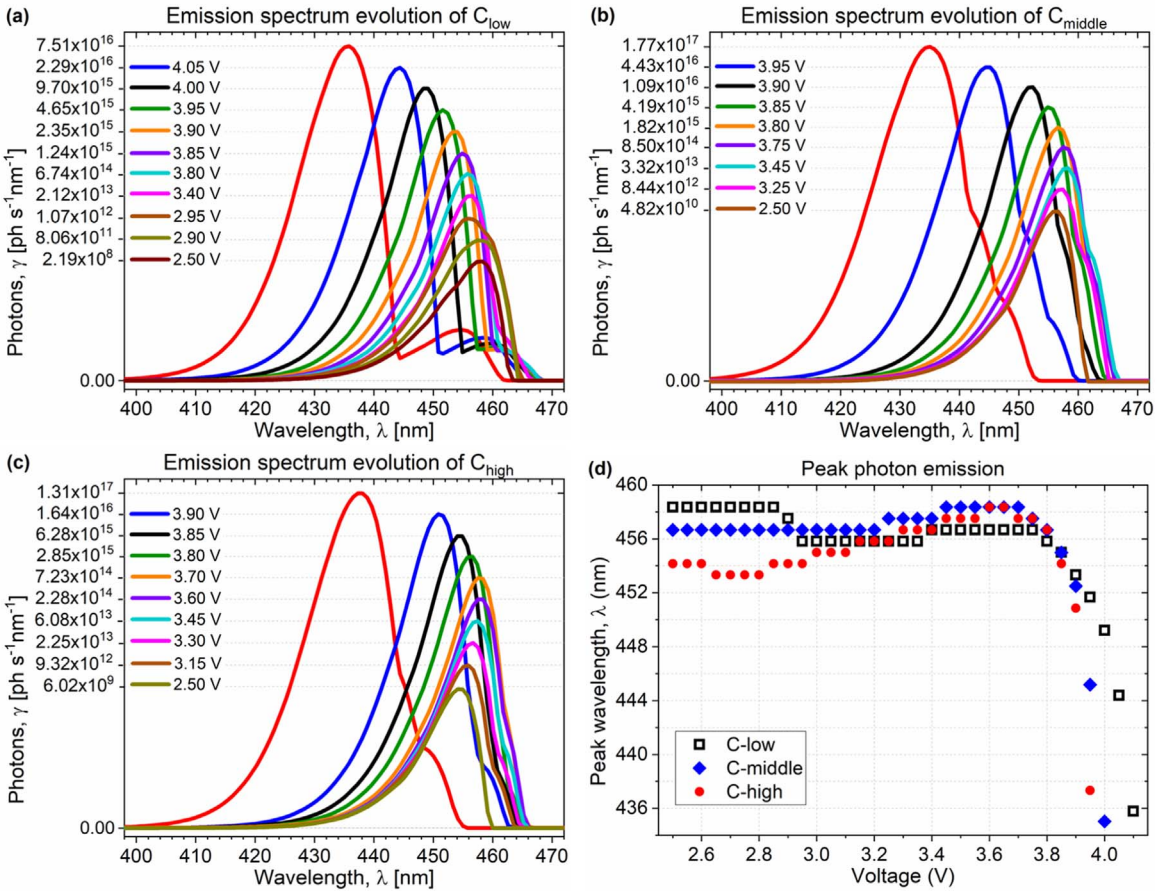

Figure 8. Spectrum evolution at different voltage points for (a) C_{low}, (b) C_{middle} and (c) C_{high}. (d) Maximum peak wavelength vs voltage for all the three concentrations the $In_{0.15}Ga_{0.85}N$/GaN LED.

and less in C_{low}, being possible to correlate it with $R_{p/n}$, since, having more carriers available implies that higher energy states are occupied, and transitions are faster and continuous at higher levels. In the three curves, it is notable that, despite the Stark effect, the energy acquired by charge carriers is so large for the last voltage points that the emission is reversed towards shorter wavelengths, resulting in the LED losing its characteristic emission color. In this sense, the last voltage points do not represent the LED's natural emission, but rather a consequence of the energetic increase in carriers, varying the emission at the expense of continued operation and maintaining high efficiencies before burning out the device. Hence, at each concentration, the LED's characteristic emission color was calculated using the wavelengths obtained from 2.50 V to 3.90 V, resulting in $\hat{\lambda}_{low} = (456.7 \pm 1.2)$ nm, $\hat{\lambda}_{middle} = (457.0 \pm 1.2)$ nm and $\hat{\lambda}_{high} = (455.4 \pm 1.8)$ nm. The conclusion is that C_{middle} has the most similar wavelength to the reference. The voltage range mentioned above to obtain the average wavelength corresponds to a different current range for each concentration, as shown in the first three plots of Fig. 7. For C_{low}, C_{middle} and C_{high} the corresponding currents are (0.22–-18.79) mA, (0.08–63.25) mA, and (0.07–85.48) mA, respectively. This is important because Lee et al.[20] mentions that reference device has a stable and uniform peak emission of $\lambda = 460$ nmin the (0–100) mA current range, which is not observed in our simulations; therefore, the prolonged stability of this emission peak is questioned. To reach the highest efficiency of 82.5% in our work, the emission peak stability was lost for currents higher than 63 mA, resulting in a violet shift of $\Delta\lambda = 21.6$ nm.

As mentioned earlier, the LED emission spectrum is formed by several Lorentzian peaks. Figure 9 provides the curve deconvolutions for each concentration at 3.50 V. The analysis of energy transitions indicates the existences of three principal photons between ($e_5 \rightarrow lh_5$) and ($e_6 \rightarrow hh_6/lh_6$), as well as a secondary photon with excessive energy at ($e_4 \rightarrow so_4$) for C_{low} and C_{middle}. For C_{high} the secondary photon is between ($e_7 \rightarrow lh_7$) as shown in Table III. Since, in simulations, there is not degeneration of *hh* and *lh* bands, deconvolution is able to separate both emission peaks in ($e_6 \rightarrow hh_6/lh_6$) transitions. Since the energy difference between these transitions is of 6.13, 9.42, and 10.35 meV for C_{low}, C_{middle}, and C_{high} respectively, the similarity among the calculated peaks with those of the deconvolution is gradually lost as the above-mentioned energy difference is smaller. Figure 9a presents three peaks from the four emissions of C_{low}, as Table III indicates, the longest emission ($\lambda = 463.7$ nm) does not appear in deconvolution, because the number of emitted photons is low. The fit peak with smallest error is for the ($e_4 \rightarrow so_4$) emission; thus, the transition occurs even if it seems unusual. Figure 9b displays the C_{middle} spectrum, where the four peaks correspond to its emissions. All four fits have very small errors, but Fit Peak 2 achieves very high accuracy with the ($e_6 \rightarrow lh_6$) transition. Again, the absence of the longer emission is observed in Fig. 9c for C_{high}. Unlike the other simulations, in this one, the most energetic emission corresponds to a transition between Γ and *hh* bands, since the *so* sub-band for this concentration is further from the top of the valence band. This can be explained by recalling that the high concentration of n-type and p-type dopants in the claddings brings quasi-Fermi levels closer to the edge of the conduction and valence bands, entering subsequently to the current equations to get the carrier density and after to the Poisson equation, modifying the potential. Thus, when the Schrödinger equation is solved, the eigenstates associated with the active layer are varied, facilitating the fundamental transitions.

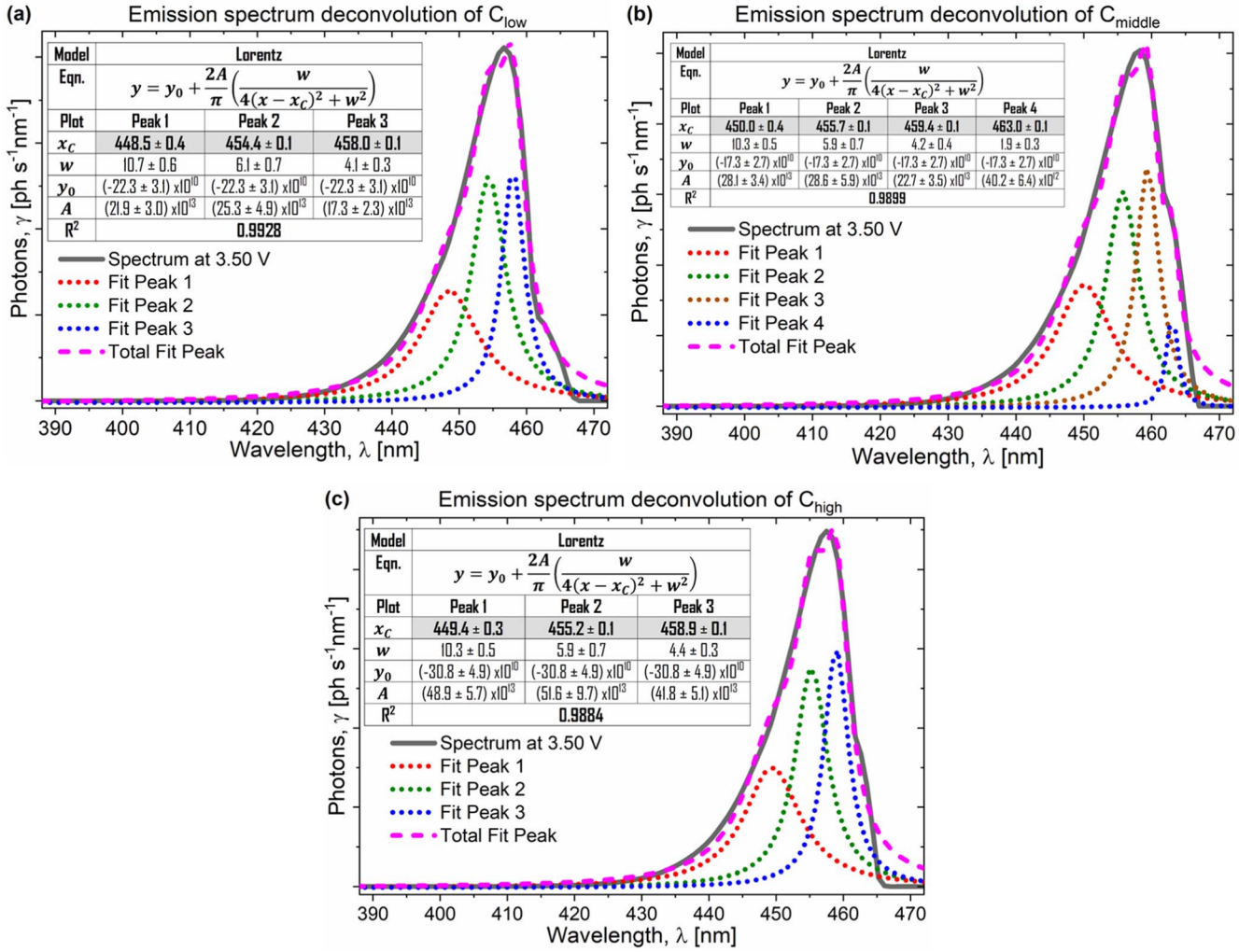

Figure 9. Emission spectrum deconvolution of (a) C_{low}, (b) C_{middle}, and (c) C_{high} at 3.50 V in the $In_{0.15}Ga_{0.85}N$/GaN LED.

Table III. Energy transitions and photon emission for the three doping concentrations in the $In_{0.15}Ga_{0.85}N$/GaN LED.

Transition	C_{low}	C_{middle}	C_{high}
$e_5 \rightarrow lh_5$ [meV]	2673.97	2669.39	2672.50
λ_{trans} [nm]	463.7	464.5	464.0
λ_{Fit} [nm]	Not shown	463.0	Not shown
Error [%]	—	0.32	—
$e_6 \rightarrow hh_6$ [meV]	2690.90	2711.15	2711.14
λ_{trans} [nm]	460.8	457.4	457.4
λ_{Fit} [nm]	458.0	459.4	458.9
Error [%]	0.61	0.44	0.34
$e_6 \rightarrow lh_6$ [meV]	2697.02	2720.57	2721.49
λ_{trans} [nm]	459.8	455.8	455.6
λ_{Fit} [nm]	454.4	455.7	455.2
Error [%]	1.18	0.02	0.09
Another [meV]	$e_4 \rightarrow so_4$	$e_4 \rightarrow so_4$	$e_7 \rightarrow hh_7$
	2776.71	2769.13	2800.97
λ_{trans} [nm]	446.6	447.8	442.7
λ_{Fit} [nm]	448.5	450.0	449.4
Error [%]	0.44	0.50	1.51

In summary, C_{middle} shows the best results among the three concentrations studied. Starting with its electrical characteristics, it achieves a smaller ideality factor, like the reference device in the high photocurrent region. Also, C_{middle} has the fastest photocurrent activation, which is confirmed by the recombination plot and R_{rad}^{tot}. Although C_{high} achieves higher R_{rad}^{tot} values once the radiative processes are activated, it also has high non-radiative recombination values which will degrade device performance in the long term. Additionally, C_{middle} presents a more balanced spatial distribution of recombination within the four wells throughout regions II and III, which is inevitably reflected on the emission spectrum evolution, the stability of maximum peak wavelength, and the spectrum deconvolution, whose average wavelength and output optical power is very close to the reference values. Finally, the middle concentration results in low leakage current values and the higher IQE value.

Therefore, according to our study, the LED presented by Lee et al. is feasible if the doping concentration in the claddings is n-GaN $= 2 \times 10^{18}$ cm^{-3} and p-GaN $= 1 \times 10^{19}$ cm^{-3}, assuming an $In_xGa_{1-x}N$ alloy with indium relative content of $x = 0.15$. This results in an LED with well-defined transport mechanisms, whose ideality factor was $n^{III}_{C_{middle}} \approx 4.3$ in the most active photocurrent region and a cut-in voltage of $V_{cut-middle} = 3.90$ V. Low leakage currents, high R_{rad} values, and an IQE as high as 82.5% at room temperature were also achieved. Furthermore, a stable average wavelength of $\hat{\lambda} = (457.0 \pm 1.2)$ nm with narrow FWHM in a range of (0.08–63.25) mA current was achieved, resulting from the emission of four well-defined Lorentzian peaks. At an injection current of 20 mA, the optical power and forward voltage were $\mathbb{P}_{middle} = 14.76$ mW/s and $V_{middle} = 3.81$ V, respectively. The only

inconsistency presented here is about the stability of the emission peak at high currents. Since, if a uniform and stable emission occurs in the real device even at high currents, it must be analyzed where the excess energy which is acquired by carriers is lost. This device achieves high structural quality by presenting a low defect density (TDD) $\sim 1 \times 10^6\,\mathrm{cm}^{-2}$, as was reported; thus, the wells in its band structure are sufficiently deep and steep to host carriers at various energetic levels, whose recombination will generate a more energetic photon each time the particles rise to a higher sub-band, due to increases in voltage. The device also does not have an electron blocking layer (EBL), so one would expect electrons to pass through the last GaN intrinsic barrier and enter the claddings, which could maintain a stable wavelength emission, but also lead to an efficiency droop. In addition, if carriers do not escape to the claddings, the excess energy must be lost in interband transitions, vibrations, or collisions, promoting the Joule effect, which will heat the material, rearrange the structure, and degrade its performance in the long term. Also, the authors indicate few emission losses by absorption in the bulk GaN; hence, the peak stability and its small broadening seems to be more surprising if the cladding material does not participate in any dissipative process, since as both experimental[17,70] and theoretical[2,71] studies demonstrate that the deformation and the emission peaks shift at large currents as typical features in InGaN/GaN MQW LEDs.

Conclusions

In this work, an exhaustive study was presented to explore the feasibility to obtain high internal quantum efficiency and wavelength stability in an InGaN/GaN blue LED. Simulations were done in order to replicate one LED structure on freestanding GaN with high-quality material (TDD $\sim 1 \times 10^6\,\mathrm{cm}^{-2}$), sharp and well-defined interfaces, and outstanding optoelectronic properties. This defect-free materials are ideal for modeling physical properties of a device and compare the simulated results with measured data. Our goal was to find a doping concentration of claddings in order to achieve these desired parameters using the QDD model. Thus, three concentrations were tested (C_{low}, C_{middle}, C_{high}) assuming one $In_xGa_{1-x}N$ alloy with indium relative content of $x = 0.15$ for the QWs, resulting in C_{middle} showing the highest IQE of 82.5%, the most stable wavelength $\hat{\lambda} = (457.0 \pm 1.2)$ nm in the range of (0.08–63.25) mA, an optical power of $\mathbb{P} = 14.76$ mW/s, and a forward voltage of $V_{middle} = 3.81$ V at 20 mA. Thus, it was possible to reproduce the optoelectronic parameters of the device presented by Lee et al. up to 63 mA. To achieve the highest efficiency of 82.5% it is necessary to compromise the emission peak stability with a violet shift in spectrum of $\Delta\lambda = 21.6$ nm.

Acknowledgments

I thank the Instituto de Investigación en Comunicación Óptica (IICO) and Dr. Andrei Gorbatchev and Dr. Jorge Ortega-Gallegos for enriching my academic knowledge with their experimental experience. Likewise, I thank Dr. Stefan Birner who provided the license activation of Nextnano++ software.

Funding

This work was supported in part by CONACyT Mexico by Sabbatical fellowship at McMaster University and the PhD Scholarship with CVU number: 626570. Also, this work was supported by OEaD Agency at the Vienna University of Technology fellowship. L. Filipovic gratefully acknowledges financial support through the Austrian Science Fund (FWF) grant P33609-N; the Austrian Federal Ministry of Labour and Economy, the National Foundation for Research, Technology and Development and the Christian Doppler Research Association. The authors declare no conflict of interest.

ORCID

Sarai Zarate-Galvez https://orcid.org/0000-0002-4054-2512

References

1. M. Henini and M. Razeghi, *Optoelectronic Devices: III Nitrides* (Elsevier, Oxford, UK Amsterdam) (2004).
2. J. Piprek, *Nitride semiconductor devices: Principles and Simulation* (Wiley, Weinheim, Germany New York) (2007).
3. H. Morkoç, "Handbook of nitride semiconductors and devices, Vol. 1 & 2: materials properties, physics." *Growth, Electronic and Optical Processes in Nitrides* (Wiley, Weinheim, Germany New York) (2009).
4. L. Liu and J. H. Edgar, "Substrates for gallium nitride epitaxy." *Mater. Sci. Eng. R Rep.*, **37**, 61 (2002).
5. G. Li, W. Wang, W. Yang, Y. Lin, H. Wang, Z. Lin, and S. Zhou, "GaN-based light-emitting diodes on various substrates: a critical review." *Rep. Prog. Phys.*, **79**, 056501 (2016).
6. I. M. Watson, "Metal organic vapour phase epitaxy of AlN, GaN, InN and their alloys: A key chemical technology for advanced device applications." *Coord. Chem. Rev.*, **257**, 2120 (2013).
7. T. Sochacki, Z. Bryan, M. Amilusik, M. Bobea, M. Fijalkowski, I. Bryan, and Z. Sitar, "HVPE-GaN grown on MOCVD-GaN/sapphire template and ammonothermal GaN seeds: Comparison of structural, optical, and electrical properties." *J. Cryst. Growth*, **394**, 55 (2014).
8. Y. Mori, M. Imanishi, K. Murakami, and M. Yoshimura, "Recent progress of Na-flux method for GaN crystal growth." *Jpn. J. Appl. Phys.*, **58**, SC0803 (2019).
9. D. C. Look and J. R. Sizelove, "Dislocation scattering in GaN." *Phys. Rev. Lett.*, **82**, 1237 (1999).
10. Z. Liu, T. Wei, E. Guo, X. Yi, L. Wang, J. Wang, and J. Li, "Efficiency droop in InGaN/GaN multiple-quantum-well blue light-emitting diodes grown on free-standing GaN substrate." *Appl. Phys. Lett.*, **99**, 091104 (2011).
11. X. A. Cao, J. A. Teetsov, F. Shahedipour-Sandvik, and S. D. Arthur, "Microstructural origin of leakage current in GaN/InGaN light-emitting diodes." *J. Cryst. Growth*, **264**, 172 (2004).
12. Z. Benzarti, T. Sekrafi, Z. Bougrioua, and A. Khalfallah, "El Jani, BEffect of SiN Treatment on Optical Properties of In x Ga1−x N/GaN MQW Blue LEDs." *J. Electron. Mater.*, **46**, 4312 (2017).
13. T. Wang, "Topical Review: Development of overgrown semi-polar GaN for high efficiency green/yellow emission." *Semicond. Sci. Technol.*, **31**, 093003 (2016).
14. X. Zhao, B. Tang, L. Gong, J. Bai, J. Ping, and S. Zhou, "Rational construction of staggered InGaN quantum wells for efficient yellow light-emitting diodes." *Appl. Phys. Lett.*, **118**, 182102 (2021).
15. S. Zhou, Z. Wan, Y. Lei, B. Tang, G. Tao, P. Du, and X. Zhao, "InGaN quantum well with gradually varying indium content for high-efficiency GaN-based green light-emitting diodes." *Opt. Lett.*, **47**, 1291 (2022).
16. X. A. Cao, S. F. LeBoeuf, M. P. D'evelyn, S. D. Arthur, J. Kretchmer, C. H. Yan, and Z. H. Yang, "Blue and near-ultraviolet light-emitting diodes on free-standing GaN substrates." *Appl. Phys. Lett.*, **84**, 4313 (2004).
17. K. Akita, T. Kyono, Y. Yoshizumi, H. Kitabayashi, and K. Katayama, "Improvements of external quantum efficiency of InGaN-based blue light-emitting diodes at high current density using GaN substrates." *J. Appl. Phys.*, **101**, 033104 (2007).
18. E. C. Kyle, S. W. Kaun, P. G. Burke, F. Wu, Y. R. Wu, and J. S. Speck, "High-electron-mobility GaN grown on free-standing GaN templates by ammonia-based molecular beam epitaxy." *J. Appl. Phys.*, **115**, 193702 (2014).
19. M. Lee, D. Mikulik, and S. Park, "The investigation of in situ removal of Si substrates for freestanding GaN crystals by HVPE." *RSC Adv.*, **8**, 12310 (2018).
20. M. Lee, M. Yang, K. M. Song, and S. Park, "InGaN/GaN blue light emitting diodes using freestanding GaN extracted from a Si substrate." *ACS Photonics*, **5**, 1453 (2018).
21. M. Lee, H. Lee, K. M. Song, and J. Kim, "Investigation of forward tunneling characteristics of InGaN/GaN blue light-emitting diodes on freestanding GaN detached from a Si substrate." *Nanomaterials*, **8**, 543 (2018).
22. Nextnano Software for semiconductor nanodevices. Home Page. https://nextnano.com/index.php, last access: (2023-07-20).
23. J. Su, E. A. Armour, B. Krishnan, S. M. Lee, and G. D. Papasouliotis, "Stress engineering with AlN/GaN superlattices for epitaxial GaN on 200 mm silicon substrates using a single wafer rotating disk MOCVD reactor." *J. Mater. Res.*, **30**, 2846 (2015).
24. J. R. Chen, Y. C. Wu, S. C. Ling, T. S. Ko, T. C. Lu, H. C. Kuo, and S. C. Wang, "Investigation of wavelength-dependent efficiency droop in InGaN light-emitting diodes." *Appl. Phys. B*, **98**, 779 (2010).
25. H. Y. Ryu and W. Jun Choi, "Optimization of InGaN/GaN superlattice structures for high-efficiency vertical blue light-emitting diodes." *J. Appl. Phys.*, **114**, 173101 (2013).
26. H. Dong, T. Jia, J. Liang, A. Zhang, Z. Jia, W. Jia, and B. Xu, "Improved carrier transport and photoelectric properties of InGaN/GaN multiple quantum wells with wider well and narrower barrier." *Opt. Laser Technol.*, **129**, 106309 (2020).
27. K. Singh, A. Chauhan, S. Joshi, A. Sharma, P. Kumar, S. Singh, and M. Chouhan, "Fabrication and characterization of InGaN/GaN MQWs blue light-emitting diodes on sapphire substrate." *2013 International Conference on Microwave and Photonics (ICMAP), Dhanbad, India, December 13–15, 2013; IEEE Publisher*, p. 1.
28. J. Bai, Q. Wang, and T. Wang, "Characterization of InGaN-based nanorod light emitting diodes with different indium compositions." *J. Appl. Phys.*, **111**, 113103 (2012).
29. Y. Xing, L. Wang, Z. Wang, Z. Hao, Y. Luo, C. Sun, and H. Li, "A comparative study of photoluminescence internal quantum efficiency determination method in InGaN/GaN multi-quantum-wells." *J. Appl. Phys.*, **122**, 135701 (2017).

30. N. A. El-Masry, E. L. Piner, S. X. Liu, and S. M. Bedair, "Phase separation in InGaN grown by metalorganic chemical vapor deposition." *Appl. Phys. Lett.*, **72**, 40 (1998).
31. M. Rao, D. Kim, and S. Mahajan, "Compositional dependence of phase separation in InGaN layers." *Appl. Phys. Lett.*, **85**, 1961 (2004).
32. S. H. Baek, H. J. Lee, and S. N. Lee, "High-performance flat-type InGaN-based light-emitting diodes with local breakdown conductive channel." *Sci. Rep.*, **9**, 1 (2019).
33. S. Zarate-Galvez, A. Garcia-Barrientos, R. Ambrosio-Lazaro, M. Garcia-Ramirez, E. Stevens-Navarro, J. Plaza-Castillo, and O. Perez-Cortes, "An analysis of mobility influence in optoelectronics parameters in an InGaN/GaN blue LED." *Crystals*, **12**, 1108 (2022).
34. S. Lu, J. Li, K. Huang, G. Liu, Y. Zhou, D. Cai, and J. Kang, "Designs of InGaN Micro-LED structure for improving quantum efficiency at low current density." *Nanoscale Res. Lett.*, **16**, 1 (2021).
35. Z. H. Zhang, S. T. Tan, Y. Ji, W. Liu, Z. Ju, Z. Kyaw, and H. V. Demir, "A PN-type quantum barrier for InGaN/GaN light emitting diodes." *Opt. Express*, **21**, 15676 (2013).
36. D. Cavalcoli, A. Minj, M. A. Fazio, A. Cros, and M. Heuken, "Strain relaxation, extended defects and doping effects in InxGa1-xN/GaN heterostructures investigated by surface photovoltage." *Appl. Surf. Sci.*, **515**, 146016 (2020).
37. W. V. Lundin, A. V. Sakharov, E. E. Zavarin, M. A. Sinitsyn, A. E. Nikolaev, G. A. Mikhailovsky, and A. F. Tsatsulnikov, "Effect of carrier gas and doping profile on the surface morphology of MOVPE grown heavily doped." *GaN: Mg layers. Semicond.*, **43**, 963 (2009).
38. M. E. Zvanut, Y. Uprety, J. Dashdorj, M. Moseley, and W. Alan Doolittle, "Passivation and activation of Mg acceptors in heavily doped GaN." *J. Appl. Phys.*, **110**, 044508 (2011).
39. S. Nakamura, T. Mukai, M. S. M. Senoh, and N. I. N. Iwasa, "Thermal annealing effects on p-type Mg-doped GaN films." *Jpn. J. Appl. Phys.*, **31**, L139 (1992).
40. R. Y. Korotkov, J. M. Gregie, and B. W. Wessels, "Codoping of wide gap epitaxial III-Nitride semiconductors." *Optoelectron. Rev.*, **10**, 243 (2002), https://infona.pl/resource/bwmeta1.element.baztech-article-BWA2-0006-0095.
41. W. Lu, D. Aplin, A. R. Clawson, and P. K. Yu, "Effects of the gas ambient in thermal activation of Mg-doped p-GaN on Hall effect and photoluminescence." *J. Vac. Sci. Technol. A: Vac. Surf. Films.*, **31**, 011502 (2013).
42. S. Birner, S. Hackenbuchner, M. Sabathil, G. Zandler, J. A. Majewski, T. Andlauer, and P. Vogl, "Modeling of Semiconductor Nanostructures with nextnano." *Acta Phys. Pol. A*, **110**, 111 (2006).
43. A. Trellakis, A. T. Galick, A. Pacelli, and U. Ravaioli, "Iteration scheme for the solution of the two-dimensional Schrödinger-Poisson equations in quantum structures." *J. Appl. Phys.*, **81**, 7880 (1997).
44. A. Trellakis, T. Zibold, T. Andlauer, S. Birner, R. K. Smith, R. Morschl, and P. Vogl, "The 3D nanometer device project nextnano: Concepts, methods, results." *J. Comput. Electron.*, **5**, 285 (2006).
45. S. Birner, T. Zibold, T. Andlauer, T. Kubis, M. Sabathil, A. Trellakis, and P. Vogl, "Nextnano: general purpose 3-D simulations." *IEEE Trans. Electron Devices*, **54**, 2137 (2007).
46. A. Jüngel, "Quantum drift-diffusion equations." *Transport Equations for Semiconductors, Lect. Notes Phys. 773* (Springer, Berlin Heidelberg Berlin) p. 251 (2009).
47. T. T. Mnatsakanov, M. E. Levinshtein, L. I. Pomortseva, S. N. Yurkov, G. S. Simin, and M. A. Khan, "Carrier mobility model for GaN." *Solid-State Electronics*, **47**, 111 (2003).
48. R. Quay, C. Moglestue, V. Palankovski, and S. Selberherr, "A temperature dependent model for the saturation velocity in semiconductor materials." *Mater. Sci. Semicond. Process.*, **3**, 149 (2000).
49. C. Nextnano, (2023-07-20), https://nextnano.com/nextnanoplus/software_documentation/database/mobility_constant.htm.
50. COMSOL, (2023-07-20), https://doc.comsol.com/5.5/doc/com.comsol.help.semicond/semicond_ug_semiconductor.6.52.html.
51. AZoMaterials, Articles, (2023-07-20), https://azom.com/article.aspx?ArticleID=8367.
52. Rensselaer Polytechnic Institute, NY USA. School of Engineering, E. Fred Schubert, Educational Sources. Materials Semiconductors III-V nitridesE. Fred Schubert, (2023-07-20), https://sites.ecse.rpi.edu/~schubert/Educational-resources/Materials-Semiconductors-III-V-nitrides.pdf.
53. C. H. Swartz, R. P. Tomkins, T. H. Myers, H. Lu, and W. J. Schaff, "Demonstration of nearly non-degenerate electron conduction in InN grown by molecular beam epitaxy." *Phys. Status Solidi C*, **2**, 2250 (2005).
54. N. Ma, X. Q. Wang, S. T. Liu, G. Chen, J. H. Pan, L. Feng, and B. Shen, "Hole mobility in wurtzite InN." *Appl. Phys. Lett.*, **98**, 192114 (2011).
55. Y. Arakawa, K. Ueno, H. Imabeppu, A. Kobayashi, J. Ohta, and H. Fujioka, "Electrical properties of Si-doped GaN prepared using pulsed sputtering." *Appl. Phys. Lett.*, **110**, 042103 (2017).
56. S. Poncé, D. Jena, and F. Giustino, "Hole mobility of strained GaN from first principles." *Phys. Revi. B*, **100**, 085204 (2019).
57. C. A. Hernández-Gutiérrez, Y. L. Casallas-Moreno, V.-T. Rangel-Kuoppa, D. Cardona, Y. Hu, Y. Kudriatsev, M. A. Zambrano-Serrano, S. Gallardo-Hernandez, and M. Lopez-Lopez, "Study of the heavily p-type doping of cubic GaN with Mg." *Sci. Rep.*, **10**, 16858 (2006).
58. M. Horita, S. Takashima, R. Tanaka, H. Matsuyama, K. Ueno, M. Edo, and J. Suda, "Hall-effect measurements of metalorganic vapor-phase epitaxy-grown p-type homoepitaxial GaN layers with various Mg concentrations." *Jpn. J. Appl. Phys.*, **56**, 031001 (2017).
59. K. A. Bulashevich, O. V. Khokhlev, I. Y. Evstratov, and S. Y. Karpov, "Simulation of light-emitting diodes for new physics understanding and device design." *Proc. SPIE*, **8278**, 827819 (2012).
60. I. Vurgaftman and J. N. Meyer, "Band parameters for nitrogen-containing semiconductors." *J. Appl. Phys.*, **94**, 3675 (2003).
61. D. K. Schroder, *Semiconductor material and device characterization* 3rd ed. (Wiley, New York) p. 158 (2006).
62. R. Jian, L. Li, D. Yan, and X. Gu, "Analysis of Forward Tunnelling Current in GaN-based Blue LEDs." *Proceedings of the 2nd International Conference on Computer Science and Electronics Engineering (ICCSEE 2013), Hangzhou, China, March 22–23, 2013; Published by Atlantis Press; Advances in Intelligent Systems Research* **34**, p. 822.
63. J. J. Huang, H. C. Kuo, and S. C. Shen, "Efficiency droop in GaInN/GaN LEDs. In *Nitride Semiconductor Light-Emitting Diodes (LEDs): Materials, Technologies, and Applications*." *Woodhead Publishing Series in Electronic and Optical Materials* (Elservier, Cambrige UK) p. 299 (2017).
64. X. Jia, Y. Zhou, B. Liu, H. Lu, Z. Xie, R. Zhang, and Y. Zheng, "A simulation study on the enhancement of the efficiency of GaN-based blue light-emitting diodes at low current density for micro-LED applications." *Mater. Res. Express*, **6**, 105915 (2019).
65. E. Kioupakis, Q. Yan, D. Steiauf, and C. Van de Walle, "Temperature and carrier-density dependence of Auger and radiative recombination in nitride optoelectronic devices." *New J. Phys.*, **15**, 125006 (2013).
66. J. Cho, E. F. Schubert, and J. K. Kim, "Efficiency droop in light-emitting diodes: Challenges and countermeasures." *Laser Photonics Rev.*, **7**, 408 (2013).
67. M. Lundstrom, "Carrier Scattering." *Fundamentals of carrier transport* 2nd ed. (Cambridge University Press, Cambridge) p. 54 (2010).
68. F. Bernardini, V. Fiorentini, and D. Vanderbilt, "Spontaneous polarization and piezoelectric constants of III-V nitrides." *Phys. Rev. B*, **56**, R10024 (1997).
69. T. Takeuchi, S. Sota, M. Katsuragawa, M. Komori, H. Takeuchi, H. A. H. Amano, and I. A. I. Akasaki, "Quantum-confined Stark effect due to piezoelectric fields in GaInN strained quantum wells." *Jpn. J. Appl. Phys.*, **36**, L382 (1997).
70. Y. K. Su, G. C. Chi, and J. K. Sheu, "Optical properties in InGaN/GaN multiple quantum wells and blue LEDs." *Opt. Mater.*, **14**, 205 (2000).
71. J. Senawiratne, A. Chatterjee, T. Detchprohm, W. Zhao, Y. Li, M. Zhu, and C. Wetzel, "Junction temperature, spectral shift, and efficiency in GaInN-based blue and green light emitting diodes." *Thin Solid Films*, **518**, 1732 (2010).